SUPERORBITAL ENTRY HEAT TRANSFER INCLUDING ATOMIC LINE RADIATION AND MASSIVE BLOWING

Thesis by
Raymond B. Dirling, Jr.

In Partial Fulfillment of the Requirements
For the Degree of
Aeronautical Engineer

California Institute of Technology
Pasadena, California
June, 1968

ACKNOWLEDGEMENTS

The author expresses his appreciation to Dr. Mitch Thomas, Dr. Bill Rigdon, and Professor Lester Lees for their enlightening discussions and thoughtful comments which have had a significant influence on the development and scope of this paper.

This research was sponsored by the NASA Langley Research Center under Contract No. NAS1-7757 and by the Douglas Aircraft Company Independent Research and Development Program, entitled Entry Heat Transfer (80301-010 39113).

ABSTRACT

At superorbital reentry velocities radiative heating is the dominant mode of heat transfer to the stagnation region of blunt reentry vehicles. The radiative heat transfer rate at the wall is determined by the temperature profile through the shock layer which depends on the net radiative transport through both the viscous inner region adjacent to the wall and the outer region where convection and radiative transport processes dominate the energy transfer. When atomic line transitions are included a very small scale length for radiant energy transport is introduced which results in characteristic changes in the shock layer flow. The inclusion of atomic line transitions necessitates consideration of self-absorption of radiant energy and results in the coupling of radiant energy transport and convection and conduction transport processes even for relatively small vehicle nose radii.

In the formulation of this problem no restrictions are placed on the variation of the absorption coefficient of the medium with wavelength. As an illustrative example the effects of nose radius, wall reflectivity, and massive blowing have been computed for the shock layer flow field of a spherically blunted vehicle at 50,000 feet per second and 200,000 foot altitude in air.

TABLE OF CONTENTS

PART	TITLE	PAGE
	Acknowledgements	ii
	Abstract	iii
	Table of Contents	iv
	List of Figures	v
	List of Symbols	vii
I.	Introduction	1
II.	Differential Equations: Application to the Forward Stagnation Region of a Spherically Blunted Vehicle	3
III.	Radiant Energy Transport	7
IV.	Typical Solutions for Atmospheric Entry: V_∞ = 50,000 fps, h = 200,000 ft	11
V.	Summary	17
	References	18
	Appendix A - Gas Properties	20
	Table 1	22
	Figures	23

LIST OF FIGURES

NUMBER		PAGE
1	Coordinate System and Shock Layer Flow Field (Schematic)	23
2	Shock Layer Flow Field for 1.0 foot Nose Radius With No Blowing	24
3	Shock Layer Flow Field for 2.5 foot Nose Radius With No Blowing	25
4	Shock Layer Flow Field for 10.0 foot Nose Radius With No Blowing	26
5	Shock Layer Flow Field for 15.0 foot Nose Radius With No Blowing	27
6	Variation of Net Emission and One-Sided Fluxes Across Shock Layer With No Blowing	28
7	Spectral Radiation Incident Normal to Wall for 1.0 foot Nose Radius With No Blowing	29
8	Spectral Radiation Incident Normal to Wall for 10.0 foot Nose Radius With No Blowing	30
9	Integrated $\nabla \cdot \vec{F}_\omega$ for Shock-Layer Radiation Traveling Toward the Wall, Evaluated 0.11 cm from the Wall	31
10	Heat Transfer Rates as a Function of Nose Radius With No Blowing	32
11	Reduction in Radiative Flux to Wall Due to Radiative and Convective Coupling	33
12	Composition of Radiative Heat Flux at the Wall as a Function of Nose Radius	34
13	Shock Layer Temperature Profiles Showing the Effect of Wall Reflectivity	35
14	Uncoupled Flow Field Solution for 10.0 foot Nose Radius With Blowing	36

NUMBER		PAGE
15	Shock Layer Flow Field for 1.0 foot Nose Radius With Blowing	37
16	Shock Layer Flow Field for 10.0 foot Nose Radius With Blowing	38
17	Variation of Net Emission and One-Sided Fluxes Across Shock Layer With Blowing	39
18	Spectral Contribution to the Radiative Heat Transfer Rate for 10.0 foot Nose Radius	40
19	Absorption Coefficient of Air at 1 atm Pressure and 15000°K	41

LIST OF SYMBOLS

B_ω°	spectral intensity of black body
c_p	specific heat
$\vec{F}$	radiative flux vector
F^+	radiative flux in positive y-direction
F^-	radiative flux in negative y-direction
h	altitude
I	intensity of radiation
λ	total thermal conductivity
k_ω	linear spectral absorption coefficient
k_P	Planck mean absorption coefficient
p	pressure
q	heat transfer rate at wall
Q	λ dT/dy
r	distance from body centerline
Rey	Reynolds Number
R_N	body nose radius
s	line of sight path length
T	temperature
u	velocity parallel to body
v	velocity normal to body
V_∞	freestream velocity
x	distance normal to body

y	distance normal to body
γ	radiation-convection coupling parameter
θ	angle between y unit vector and line of sight path
μ	viscosity
ρ	density
σ	Stefan-Boltzmann constant
ω	wave number

Subscripts

c	convective
r	radiative
s	value immediately downstream of shock
t	total
ω	spectral
∞	freestream

I. INTRODUCTION

For atmospheric entry velocities above escape speed thermal radiation significantly alters the flow field about blunt entry bodies. The predominant effect of the radiance of the hot gas cap is the introduction of enthalpy gradients in the outer shock layer. Thus, when radiative transfer is important, the flow field can not be separated into the usual isoenergetic inviscid outer shock layer and a non-adiabatic viscous boundary layer. This effect has been treated by others using either the gray gas approximation[1] or polynomial expressions for the velocity and concentration profiles and numerical integration over frequency of radiation[2]. It is now well known that use of the gray gas approximation in radiative transfer calculations for high-temperature air results in serious error. Also the difficulties associated with integrating over frequency while also integrating the conservation equations are obvious (Hoshizaki and Wilson were limited to about 20 frequency points).

As a result of these difficulties many approximate techniques have been developed to solve radiative gasdynamic problems[3],[4],[5]. In general the accuracy of the various solutions is unknown since no flight experiments have been made above 36,000 fps (NASA's Project FIRE) where coupling is rather weak. In lieu of experimental data for shock layer temperatures of approximately 15,000°K and large physical size, more exact calculations retaining complete spectral detail with as few flow field approximations as possible are required. In particular atomic line emission must be included since, due to the very large

values of absorption coefficient at the center of these lines, an extremely small scale length for the radiant energy transport is introduced.

Injection into the boundary layer is unavoidable in the flight regime considered here since the heat transfer rates encountered - on the order of 10^3 watts/cm^2 - will necessitate either ablative heat shields or transpiration cooling for thermal protection. Injection of foreign gas greatly complicates the analysis procedure because the absorption coefficient of the gas-air mixture, on which the radiative transport processes critically depend, is a strong function of the species present and their concentrations. However, the first order effects of injection on the shock layer flow field structure can be determined by considering air as the injected gas, and this approach will be used here.

In the present investigation of these phenomena the primary emphasis has been on retaining as complete spectral detail as possible, thereby making full use of existing knowledge of radiative mechanisms. The shock layer flow is considered to be in local chemical and thermodynamic equilibrium for the entry conditions chosen. The energy equation is satisfied by using an iterative technique and assuming one-dimensionality of the radiation field. Molecular heat conduction and viscous momentum transport are retained across the entire shock layer. The solutions obtained reveal the details of the shock layer flow field structure and radiative transport processes as well as the convective and radiative heat transfer rates.

II. DIFFERENTIAL EQUATIONS: APPLICATION TO THE FORWARD STAGNATION REGION OF A SPHERICALLY BLUNTED VEHICLE

Consider the shock layer flow field about the forward stagnation point of a blunt body shown schematically in Figure 1. In order to account for radiative transport of energy the entire shock layer must be considered.

For steady-state, axisymmetric flow the thin shock layer equations are the following[1]:

Continuity

$$\frac{\partial(\rho r u)}{\partial x} + \frac{\partial(\rho r v)}{\partial y} = 0 \tag{1}$$

Momentum

$$\rho u \frac{\partial u}{\partial x} + \rho v \frac{\partial u}{\partial y} = - \frac{\partial p}{\partial x} + \frac{1}{r} \frac{\partial}{\partial y} (r\mu \frac{\partial u}{\partial y}) \tag{2}$$

$$\frac{\partial p}{\partial y} = 0 \tag{3}$$

Energy

$$\rho u c_p \frac{\partial T}{\partial x} + \rho v c_p \frac{\partial T}{\partial y} = u \frac{\partial p}{\partial x} + \mu (\frac{\partial u}{\partial y})^2 + \frac{1}{r} \frac{\partial}{\partial y} (r\lambda \frac{\partial T}{\partial y}) - \nabla \cdot \vec{F} \tag{4}$$

where $\vec{F}$ is the radiative flux vector. The coupling between the radiative energy transport and the other processes is evidenced by the inclusion of the net radiative energy loss per unit volume, $\nabla \cdot \vec{F}$, in the energy equation. The evaluation of this term is considered in Section III.

These equations can be reduced to ordinary differential equations valid near the stagnation streamline by noting that to first order in x

$$r \tilde{=} x$$

and

$$u(x, y) \tilde{=} xu(y) \quad .$$

The continuity equation then becomes

$$u = -\frac{x}{2\rho} \frac{d}{dy} (\rho v) \quad . \tag{5}$$

Substituting Eq. 5 in the momentum and energy equation and neglecting terms of order x yields the following:

Momentum and Continuity

$$\frac{d}{dy} \left[\mu \frac{d}{dy} \left(\frac{1}{\rho} \frac{d(\rho v)}{dy}\right)\right] - (\rho v) \frac{d}{dy} \left(\frac{1}{\rho} \frac{d(\rho v)}{dy}\right)$$

$$- \left[4\rho_\infty \left(1 - \frac{\rho_\infty}{\rho_s}\right) \frac{du_s}{dx} - \frac{\rho}{2} \left(\frac{1}{\rho} \frac{d(\rho v)}{dy}\right)^2\right] = 0 \tag{6}$$

Energy

$$\rho v c_p \frac{dT}{dy} = \frac{d}{dy} \left(\lambda \frac{dT}{dy}\right) - \nabla \cdot \vec{F} \tag{7}$$

where, after Reference 1, $\partial p/\partial x$, has been replaced by its value immediately behind a spherical shock near the stagnation streamline.

The boundary conditions on Eqs. 6 and 7 are at y = 0

$$\rho v = \rho_w v_w$$

$$\frac{1}{\rho} \frac{d(\rho v)}{dy} = 0$$

$$T = T_w$$

and at $y = \delta$

$$\rho v = - \rho_\infty V_\infty$$

$$\frac{1}{\rho} \frac{d(\rho v)}{dy} = - 2 \frac{du_s}{dx} = - 2 \frac{V_\infty}{R_N}$$

$$T = T_s$$

where δ, the shock stand-off distance, is to be determined from the solution.

For cases in which blowing is absent integration of Eqs. 6 and 7 is started at the wall by assuming values for the convective heat transfer rate and shear stress and continues away from the wall until the shock ($\rho v = -\rho_\infty V_\infty$) is reached. Tabular values of the net emission as a function of ρv are used in the solution of the energy equation to obtain solution curves for the temperature. Boundary conditions on T and u at the shock are matched by repeated adjustment of the convective heat transfer rate and shear at the wall.

When massive blowing is considered some modification to this procedure is required. Integral solutions of both the momentum and energy equations can be easily obtained. For instance, the solution of the energy equation is

$$Q(y) = \exp\left[\int_o^y \rho v \frac{c_p}{\lambda} ds\right] \left\{ \int_o^y \frac{\nabla \cdot \vec{F}(s) ds}{\exp\left[\int_o^s \rho v \frac{c_p}{\lambda} d\xi\right]} + Q(o) \right\}$$

where

$$Q = \lambda \frac{dT}{dy} \quad .$$

This equation shows that small errors in the choice of Q(o) cause the computed value of Q(y) to depart exponentially from the correct value of Q(y) in regions where ρv is greater than zero. Since $\rho v c_p/\lambda$ is of the order of 1 to 10 for the case considered here, the error grows very fast. The situation is exactly the same when the momentum equation is considered. In general the requirement that both of these equations be integrated simultaneously means that varying initial values of the convective heat transfer rate and the shear stress at the wall is not a practical way to satisfy boundary conditions imposed at the shock. In order to overcome this difficulty, numerical integration is started at $\rho v = 0$ (i.e., away from the wall) and proceeds in both directions. While this procedure eliminates the numerical integration instability in the blown region, it requires that four initial values be iterated upon ($T(\rho v = 0)$, $u(\rho v = 0)$, $dT/dy(\rho v = 0)$ and the shear stress at $\rho v = 0$) and that the boundary conditions on T and u be matched at both the wall and the shock. The addition of two more initial values quadruples the complexity of the iteration procedure required since there are now sixteen derivatives of the end values instead of four as when integration is started at the wall.

III. RADIANT ENERGY TRANSPORT

In order to evaluate the net radiant energy emission, $\nabla \cdot \vec{F}$, the actual shock layer geometry is replaced by a plane parallel layer, infinite in extent, with properties varying only in the y-direction. The net emission from this layer is then given by

$$\nabla \cdot \vec{F} = \frac{dF(y)}{dy} \tag{8}$$

where F denotes the flux of radiant energy in the y-direction. This approximation is in accord with the results of Cheng[6], who computed the flux in the x-direction employing the gray gas assumption but not the plane parallel shock layer approximation. His results indicate that the contribution to $\nabla \cdot \vec{F}$ from the x-direction flux is small. The plane parallel shock layer approximation is more valid when atomic lines and ultraviolet photoionization continuum are included since that part of the radiation spectrum behaves in an opaque manner (except near the boundaries) and only radiation from nearby points is important. Splitting the flux into positive and negative y-components results in

$$F(y) = F^{+}(y) - F^{-}(y) \tag{9}$$

where

$$F^{+}(y) = -2\pi \int_{\theta=0}^{\pi/2} \int_{0}^{\infty} I_{\omega}(y, \theta) \cos\theta \, d\omega d(\cos\theta) \tag{10a}$$

and

$$F^{-}(y) = 2\pi \int_{\theta=\pi/2}^{\pi} \int_{0}^{\infty} I_{\omega}(y, \theta) \cos\theta \, d\omega d(\cos\theta) \quad . \tag{10b}$$

In Eq. 10 θ is the angle between a line of sight path from the edge of the layer to the y-station and the y-vector along the stagnation streamline (see Figure 1). I_ω is the spectral intensity of radiation at y traveling in the θ direction and is given by integration of the Lambert-Bouguer law for a non-scattering medium

$$\frac{dI_\omega}{ds} = k_\omega (B^\circ_\omega - I_\omega) \tag{11}$$

where s denotes distance along the line of sight path.

The boundary conditions on Eq. 11 depend on the optical properties of the wall. Three limiting wall conditions are considered here. The usual condition imposed is that the wall is perfectly transparent. This implies that

$$I_\omega(0,\theta) = 0 \quad \text{for all } \omega \text{ and } 0 \leq \theta \leq \pi/2 \tag{12a}$$

The other two limiting cases are a perfectly black wall or a perfectly reflecting wall. The radiative boundary conditions for these two cases are as follows:

black wall

$$I_\omega(0,\theta) = B^\circ_\omega(T_w) \quad \text{for all } \omega \text{ and } 0 \leq \theta \leq \pi/2 \tag{12b}$$

reflecting wall

$$I_\omega(0,\theta) = I_\omega(0,\pi-\theta) \quad \text{for all } \omega \text{ and } 0 \leq \theta \leq \pi/2 \tag{12c}$$

Eqs. 12a, b, c set the initial conditions for the intensity of radiation leaving the wall. The boundary conditions for the radiation traveling toward the wall are usually set by the conditions of a transparent shock and no emission from the freestream ahead of the shock. However, it should be recognized that some fraction of the radiation

that leaves the shock layer will be absorbed by the freestream thus raising its temperature and increasing its emission. A quantitative estimate of this effect has yet to be made and the assumption of no emission from the freestream will be retained for this investigation. The boundary condition for the radiation traveling toward the wall is thus

$$I_\omega(\delta,\theta) = 0 \quad \text{for all } \omega \text{ and } \pi/2 < \theta \leq \pi \quad . \tag{13}$$

These equations permit the evaluation of the net emission from an elemental unit volume of gas, provided the temperature profile is known. Since the temperature depends on the value of the net emission, which in turn depends on the temperature profile across the entire shock layer, an iterative technique is employed in this investigation. Assumed tabular values of the net emission as the function of ρv are used in the solution of the conservation equations to obtain solution curves for the temperature. The first set of these values is obtained by computing $\nabla \cdot \vec{F}$ for the uncoupled temperature profile, i.e., the solution of the conservation equations with $\nabla \cdot \vec{F} \equiv 0$. With the temperature profile computed, Eqs. 8, 9, 10, and 11 are used with the appropriate boundary conditions at the wall to compute new values for the net emission. Eq. 11 is solved using second-order Rugge-Kutta for the most part. However, when the intensity at any frequency becomes close to the black-body value, the asymptotic form of Eq. 11

$$I_\omega \simeq B^\circ_\omega - \frac{1}{k_\omega}\frac{\partial B^\circ_\omega}{\partial s}$$

is used. The use of this asymptotic expression for the intensity allows large integration intervals to be used, typically about 1/100th the shock layer thickness, rather than intervals of the order $1/k_\omega$

required for integration stability if the full equation were retained. The intensity for eight different slant directions through the layer is found by integration along each path; fluxes are then determined by Gaussian quadrature. This cycle is repeated until the input and output net emission curves converge.

IV. TYPICAL SOLUTIONS FOR ATMOSPHERIC ENTRY: V_∞ = 50,000 fps, h = 200,000 ft

The methods described in Sections II and III have been used to obtain solutions for atmospheric entry at 50,000 feet per second and 200,000 feet altitude with a wall temperature of 2000°K. The air properties used are described in the Appendix. Transport of radiant energy by atomic line transitions is included. In the following discussion of the results obtained particular attention is paid to the effect of the inclusion of atomic line radiation.

Flow Field Solutions

The effects of radiant energy transport on the shock layer structure for various nose radii and a transparent wall are shown in Figures 2, 3, 4, and 5. Emission of thermal radiation results in a continual decrease in temperature as the gas flows toward the wall. The sharp decline in temperature near the shock is due to the build up of intensity in the vacuum ultraviolet spectrum to the black body limit. This occurs a very small distance behind the shock wave due to the large values of the k_ω for the atomic lines. The lower temperature throughout the shock layer results in higher density and a corresponding decrease in the shock stand-off distance. Shear stress at the wall is increased and the velocity boundary layer thickness decreased due to the coupling of radiation and convection energy transport modes.

Radiant Energy Transport

The radiant energy transport is shown in Figure 6 for a 10 foot nose radius. The net emission at the shock is only slightly larger than

the transparent emission into 2π steradians, i.e., $2k_p(T_s)\,\sigma T_s^4$. As the flux traveling toward the wall, F^-, builds up, the net emission falls rapidly due to self absorption. The extremely large value of $\nabla \cdot \vec{F}$ at the shock (about 250,000 watts/cm^3) produces the steep declines in temperature at the shock wave evidenced in the flow field solutions. Since the temperature decreases continuously as the gas flows toward the body, F^- does not increase monotonically with increasing distance from the shock. The absorption spike close to the wall is due entirely to absorption of the F^- flux in the boundary layer. Because of the small thickness of the boundary layer, however, the reduction of the radiative heat transfer rate at the wall is small. For large nose radii the conversion of radiative to convective energy in the boundary layer has a significant effect on the convective heat transfer rate.

Figures 7 and 8 present the spectral radiation incident normal to the wall for nose radii of 1 and 10 feet, respectively. The centers of the vacuum ultraviolet lines are seen to be strongly self-absorbed while the wings contribute significantly to the flux at the wall. The infrared and visible lines, though not self-reversed, are somewhat self-absorbed at the larger nose radius.

Figure 9 shows the contribution to the net emission from the flux in the negative y-direction at a position 0.11 cm from the wall for the 10 foot nose radius. At this position the atomic lines have already been self-reversed and the dominant mode of radiant energy transport is ultraviolet merged-line and photoionization continuum absorption.

Heat Transfer Rates

The dependence of the radiative and convective heating rates on nose radius without blowing is shown in Figure 10. The dashed lines indicate the uncoupled heating rates, obtained by ignoring the radiation term in the energy equation. There are two compensating effects tending to perturb the convective heat transfer rate; the reduced enthalpy potential due to radiative cooling tends to decrease the convective heating rate, while radiant energy absorption in the boundary layer tends to increase it. When atomic lines are considered the latter effect dominates except at small nose radii where boundary layer absorption is small. However, if atomic line radiation is neglected these effects tend to cancel as shown in Reference 2.

As discussed previously, the radiative flux at the wall is reduced due to radiative cooling, shock layer absorption, and boundary layer absorption; boundary layer absorption is relatively unimportant except when large blowing rates are considered. These mechanisms provide substantial reductions in the radiative flux to the surface as shown in Figure 11. Here the reduction in radiative heat transfer rate is correlated with γ, the ratio of total uncoupled radiant energy loss to the total available freestream energy. The inclusion of atomic lines is seen to enhance the reduction in radiative heating through the mechanism of increased temperature drop immediately behind the shock wave. A summary of the heat transfer rates obtained for all cases investigated is given in Table 1.

As shown in Figure 10 the radiative heat transfer does not increase monotonically with increasing nose radius. Radiative heating is

maximum for approximately an 11 foot nose radius at the flight conditions considered here. Figure 12 shows that this result is due to a decrease in the flux from the strong lines and ultraviolet portion of the spectrum reaching the wall. This effect can be traced to the lower temperature at the edge of the boundary layer with increasing radius due to radiative cooling.

Wall Reflectivity

The influence of wall reflectivity is shown in Figure 13. The temperature profile for the 10 foot nose radius shock layer with a totally reflecting wall (wall is perfectly reflecting at all wave lengths) is compared to that of a transparent wall. The totally reflecting wall is the limit case and illustrates the maximum effect due to wall reflectivity. The enthalpy potential across the boundary layer is increased due to absorption of the reflected flux and the convective heat transfer rate is increased. Since almost half of the radiant energy incident on the wall is vacuum-ultraviolet, for which all materials are nearly black, the totally reflecting wall does not represent any real surface. Of more practical concern is the effect of totally black walls. Calculation of the net radiant emission assuming a totally black wall results in values identical (within the accuracy of the calculations) to those obtained for transparent walls. This result is not surprising since the radiative flux emitted from the cold wall is much less than the flux from the high temperature shock layer. It can be concluded then that the radiative boundary conditions at the wall have a negligible effect on the gas cap radiative transfer and the transparent wall assumption is sufficient for computing the flow field solution.

Massive Blowing

Strong blowing solutions are especially important at high entry velocities because radiative heating will induce massive ablation of the vehicle surface. Thus, it is imperative to understand the effects of large blowing rates on the shock layer flow field structure and the attendant changes in radiative and convective heat transfer rates. Ideally, of course, one would like to carry out this investigation using radiative and transport properties for the blown gas mixture which correspond to the complex molecules present in the ablation products of most heat shield material.

The blowing rate used in the present study corresponds to what would be a classical shear layer ($\rho_w v_w \sqrt{Rey_s}/\rho_\infty V_\infty >> 1$) solution if radiative coupling were neglected. This is illustrated in Figure 14 which shows the temperature and tangential velocity profiles obtained by integrating the conservation equations with $\nabla \cdot \vec{F}$ set to zero. The region from the wall to about y = 0.9 cm has the properties of constant non-zero shear (as also found in Reference 7) and temperature; the region of maximum shear is displaced from the wall by the same amount.

When radiant energy transport is included strong reabsorption by the cooler injected gas results in the flow fields shown in Figures 15 and 16 for 1 foot and 10 foot nose radii, respectively. For the 10 foot case convective heat transfer is increased from zero (for the uncoupled profile) to 135 watts/cm^2 and the radiative heating reduced about 18% to 4322 watts/cm^2. If the blown gas were composed of ablation products including complex molecules which have sustantially

larger absorption coefficients than air, the conversion of radiative to convective energy would be enhanced and the radiative heating further reduced.

The radiative energy transport for this case is shown in Figure 17. It is seen that there is a net absorption of radiant energy through the injected gas region causing F^{-} to decrease significantly from its maximum value at y/δ approximately equal to one-half. A comparison of the integral of the flux incident on the wall as a function of ω

$$\int_{o}^{\omega} F_{\omega}^{-}(o)dw \quad ,$$

for the blowing and no-blowing ten-foot nose radius cases is shown in Figure 18. It is evident from these curves that the reduction in the radiative heat transfer to the wall for the blowing case is due to absorption of radiation in the merged ultraviolet lines and photoionization continuum by the blown gas.

V. SUMMARY

The stagnation-point shock-layer equations have been solved using detailed spectral calculation of the radiative-convective coupling. Atomic lines are included in the description of the absorption coefficient and their spectral structure is retained throughout the calculation procedure. The solutions obtained indicate that the inclusion of atomic lines enhances the radiative cooling effect resulting in decreased radiative flux at the wall. However, slightly increased absorption in the boundary layer causes the convective heat transfer rates to increase above the nominal value that would be obtained if radiant energy transport were neglected.

The solutions obtained with strong blowing indicate that radiant energy transport can strongly modify the flow field structure in the blown gas region through absorption in the ultraviolet portion of the spectrum. Significant reductions in the radiative heat transfer rate occur due to this absorption.

The effect of radiative boundary conditions at the wall on shock layer structure was considered and found to be small for realistic entry body properties.

REFERENCES

1. Howe, J. T. and Viegas, J. R., "Solutions of the Ionized Radiating Shock Layer, Including Reabsorption and Foreign Species Effects, and Stagnation Region Heat Transfer," NASA TR R-159 (1963).

2. Hoshizaki, H. and Wilson, K. H., "Convective and Radiative Heat Transfer During Superorbital Entry, "AIAA J., Vol 5, 25-35 (1967).

3. Anderson, Jr., J. D., "Non-gray Radiative Transfer Effects on the Radiating Stagnation Region Shock Layer and Stagnation Point Heat Transfer," NOLTR 67-104 (1967).

4. Chapman, G. T., "Heat Transfer in the Stagnation-Point Laminar Boundary Layer with Mass Transfer and Radiant Energy Absorption," Proceedings of the 1967 Heat Transfer and Fluid Mechanics Institute, Stanford University Press, 163-188 (1967).

5. Dirling, Jr., R. B., Rigdon, W. S., and Thomas, M., "Stagnation-Point Heating Including Spectral Radiative Transfer," Proceedings of the 1967 Heat Transfer and Fluid Mechanics Institute, Stanford University Press, 141-162 (1967).

6. Cheng, P. and W. G. Vincenti, "Inviscid Radiating Flow Over a Blunt Body," Report SUDAAR No. 278, Stanford, Calif., Stanford University (1966).

7. Kubota, T., and Fernandez, F. L., "Boundary-Layer Flows with Large Injection and Heat Transfer," AIAA J., Vol. 6, 22-28 (1968).

8. Thomas, M., "The Spectral Linear Absorption Coefficients of Gases--Computer Program SPECS (H189)," Report DAC-59135, Santa Monica, California, Douglas Aircraft Company, Inc. (1966).

9. Wiese, W. L., Smith, M. W., and Glennon, B. M., "Atomic Transition Probabilities," Vol. I, Hydrogen Through Neon, National Bureau of Standards, NSRDS-NBS 4 (1966).

10. Griem, H. R., Plasma Spectroscopy, McGraw-Hill Book Co., New York (1964).

11. Stewart, J. C., and Pyatt, K. D., Jr., "Theoretical Study of Optical Properties - Photon Absorption Coefficients, Opacities, and Equations of State of Light Elements, Including the Effect of Lines," Report GA-2528, Vol. I (AFSWC-TR-61-71, Vol. I), General Atomic Division, General Dynamics Corporation (1961).

12. Martinez, M. R., "Description of Computer Program H187 - Thermochemical Equilibrium Properties of Multicomponent Systems, and H289 - Statistical Thermodynamic Properties of Single Gas Species," DAC-59133, Santa Monica, California, Douglas Aircraft Company, Inc., (1967).

13. Cruise, D. R., "Notes on the Rapid Computation of Chemical Equilibrium," J. Chem. Phys. 68, 3797-3802 (1964).

14 Rigdon, W. S., "A Computer Code for Calculation of Transport Properties of High-Temperature Gases," DAC-59134, Santa Monica, California, Douglas Aircraft Co. (in preparation).

15. Gruszczynski, J. S. and Warren, Jr., W. R., "Study of Equilibrium Air Total Radiation," AIAA J., Vol. 5, 517-525 (1967).

Appendix A

GAS PROPERTIES

The spectral linear absorption coefficient is of critical importance for accurate calculations of the radiative heat transfer to entry vehicles. The values used in this study are those of Thomas[8]. In that work a complete description of the spectral absorption coefficient was made including band radiation, photodissociation, photoionization, photodetachment, atomic lines, and brehmsstrahlung. Atomic lines belonging to multiplets were grouped together, since for typical reentry conditions he found the spacing between lines of a particular multiplet to be usually of the same order as the line half widths. The f-numbers for the ultraviolet lines were taken from NBS[9] and for the visible lines from Griem[10]. Thomas used the hydrogenic model of Steward and Pyatt[11] to define lines close to the photoelectric edges. Lines from N, N^+, O, and O^+ are included.

Thomas has generaged the spectral linear absorption coefficient for air at approximately 2000 spectral points for temperatures from 2000°K to 60,000°K and pressures from 0.003 to 300 atmospheres. The values used in the present investigation were scaled according to pressure from the values calculated at 1 atmosphere. Figure 19 shows the values of k_ω Thomas obtained at 15,000°K and 1 atmosphere pressure.

The thermodynamic properties of air used here are those obtained by Martinez[12] from solution of the chemical equilibrium equations by the method of Cruise[13].

The transport properties were calculated by the method described in Reference 14 at the actual stagnation pressure (0.66 atmospheres). Equilibrium concentrations of 18 air species were used and the effects of charge exchange encounters were considered. The viscosity and equilibrium thermal conductivity were calculated to the second-order including the effects of thermal diffusion.

Table 1

SUMMARY OF CASES STUDIED
V_∞ = 50,000 ft/sec h = 200,000 ft
T_w = 2000°K

R_N (ft)	Wall Boundary Condition	$\frac{(\rho v)_w}{\rho_\infty V_\infty}$	q_c	q_r	q_t
1.0	Transparent	0	1212 (1324)	2629 (4935)	3841
1.0	Transparent	0.1	223 (13)	2128 (3449)	2351
2.5	Transparent	0	875 (833)	3607 (8666)	4482
10.0	Transparent	0	600 (409)	5296 (21,521)	5896
10.0	Transparent	0.1	135 (0)	4322 (11,937)	4457
10.0	Totally Reflecting	0	980	---- -------	980
10.0	Black	0	600	5296	5896
15.0	Transparent	0	522 (337)	5240 (27,945)	5762

Notes: 1. Heat transfer rates in watts/cm^2.

2. Numbers in parenthesis refer to uncoupled heat transfer rates.

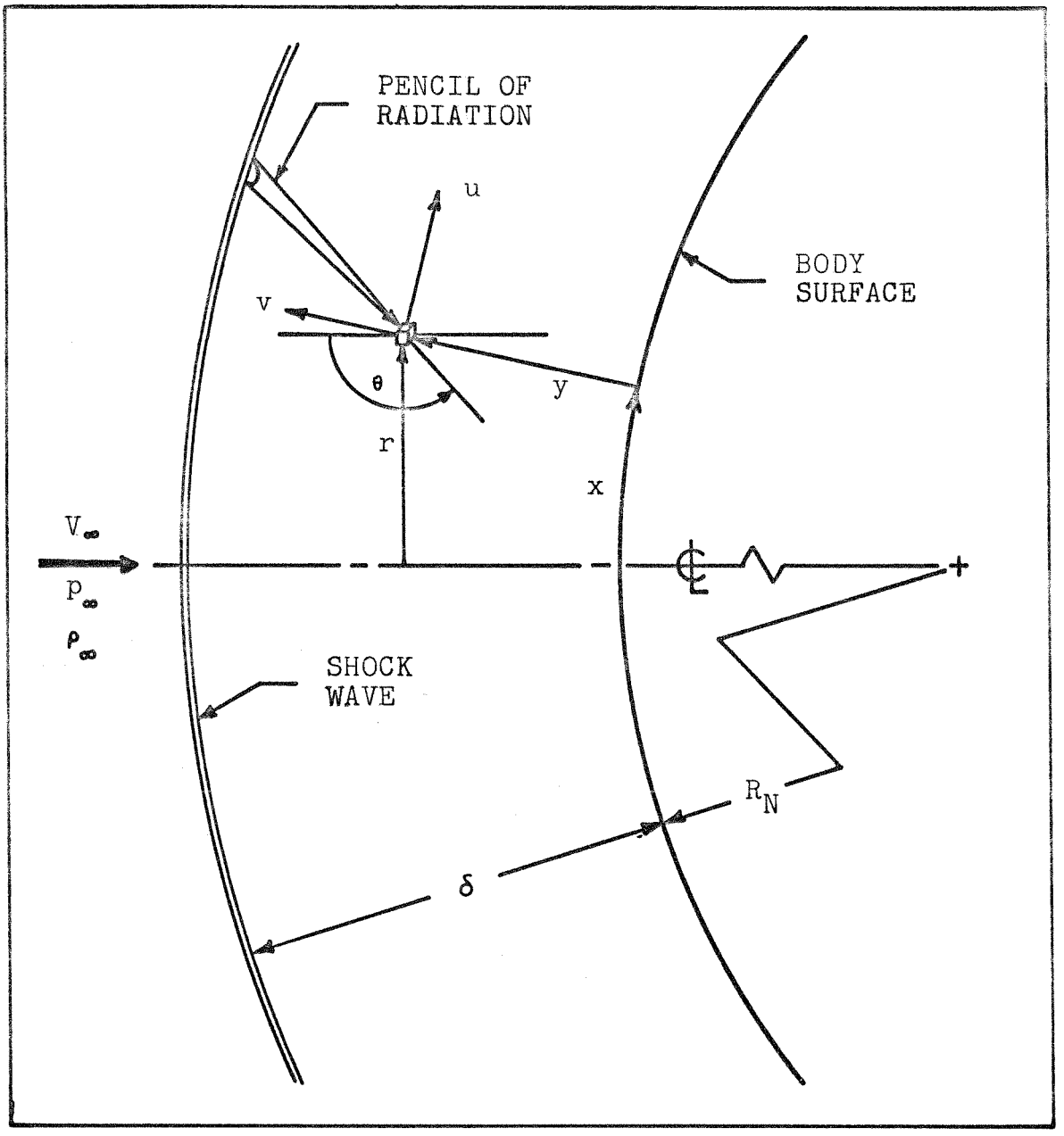

FIGURE 1. COORDINATE SYSTEM AND SHOCK LAYER FLOW FIELD (SCHEMATIC)

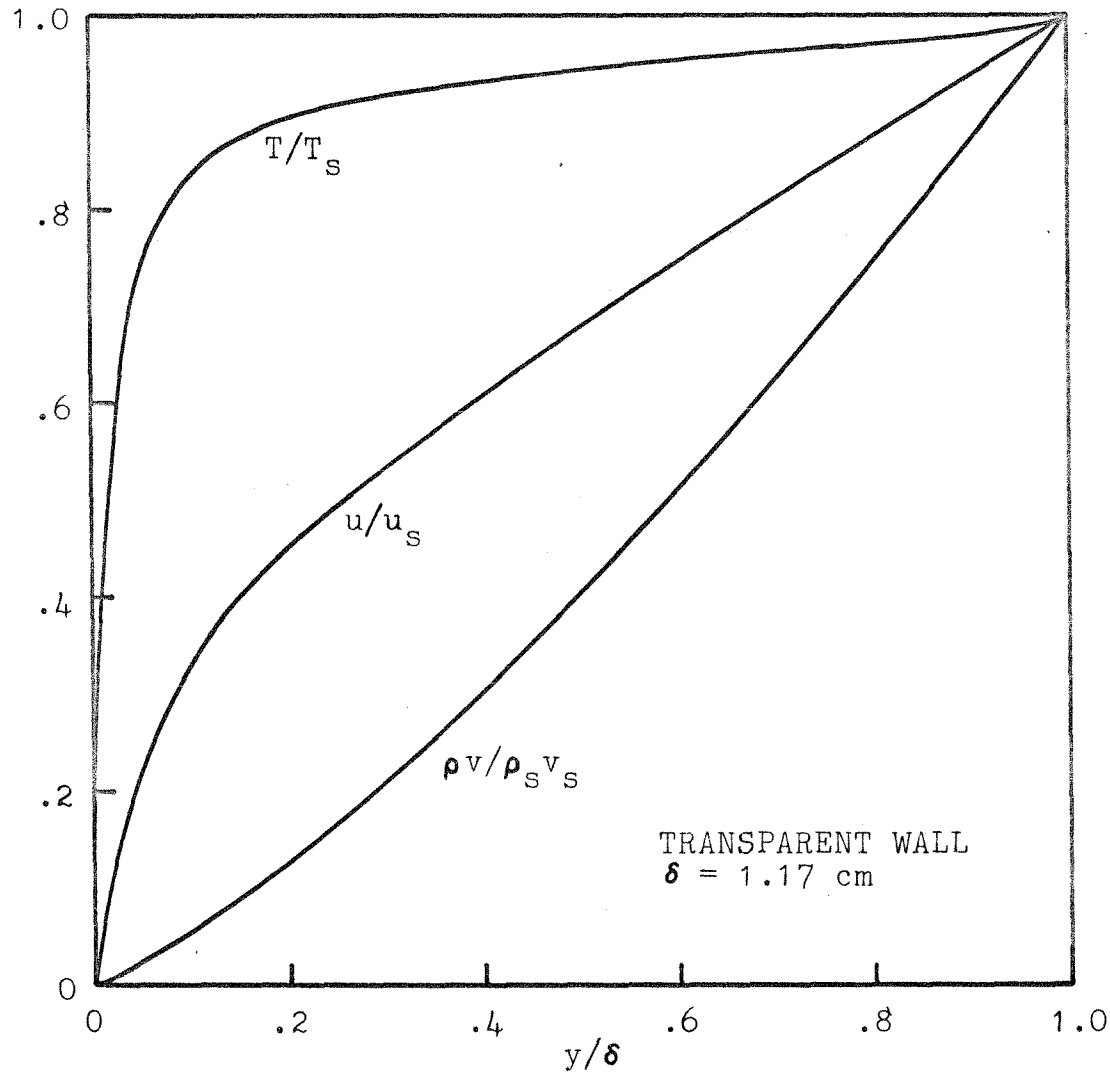

FIGURE 2. SHOCK LAYER FLOW FIELD FOR 1.0 FOOT NOSE RADIUS WITH NO BLOWING

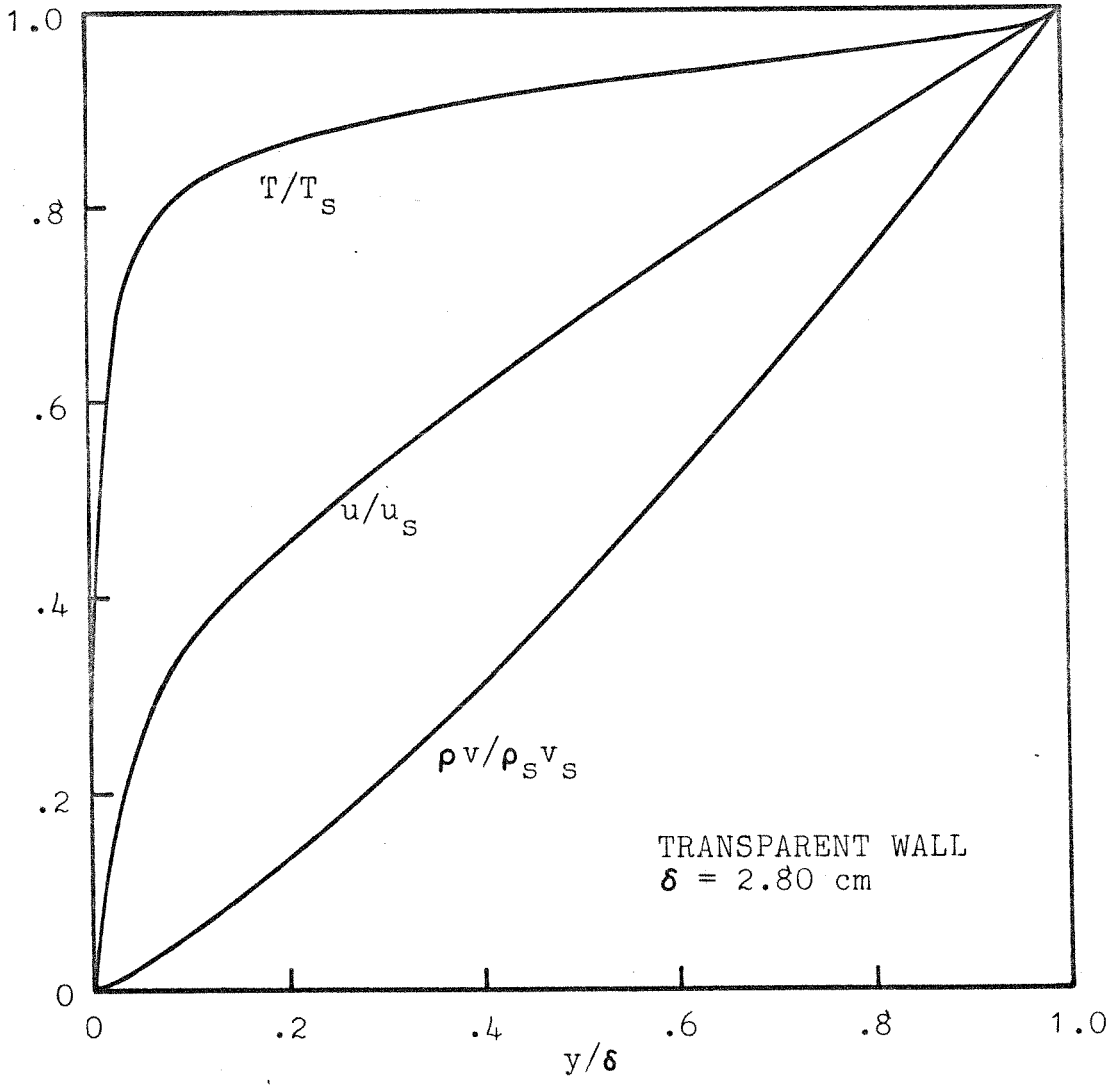

FIGURE 3. SHOCK LAYER FLOW FIELD FOR 2.5 FOOT NOSE RADIUS WITH NO BLOWING

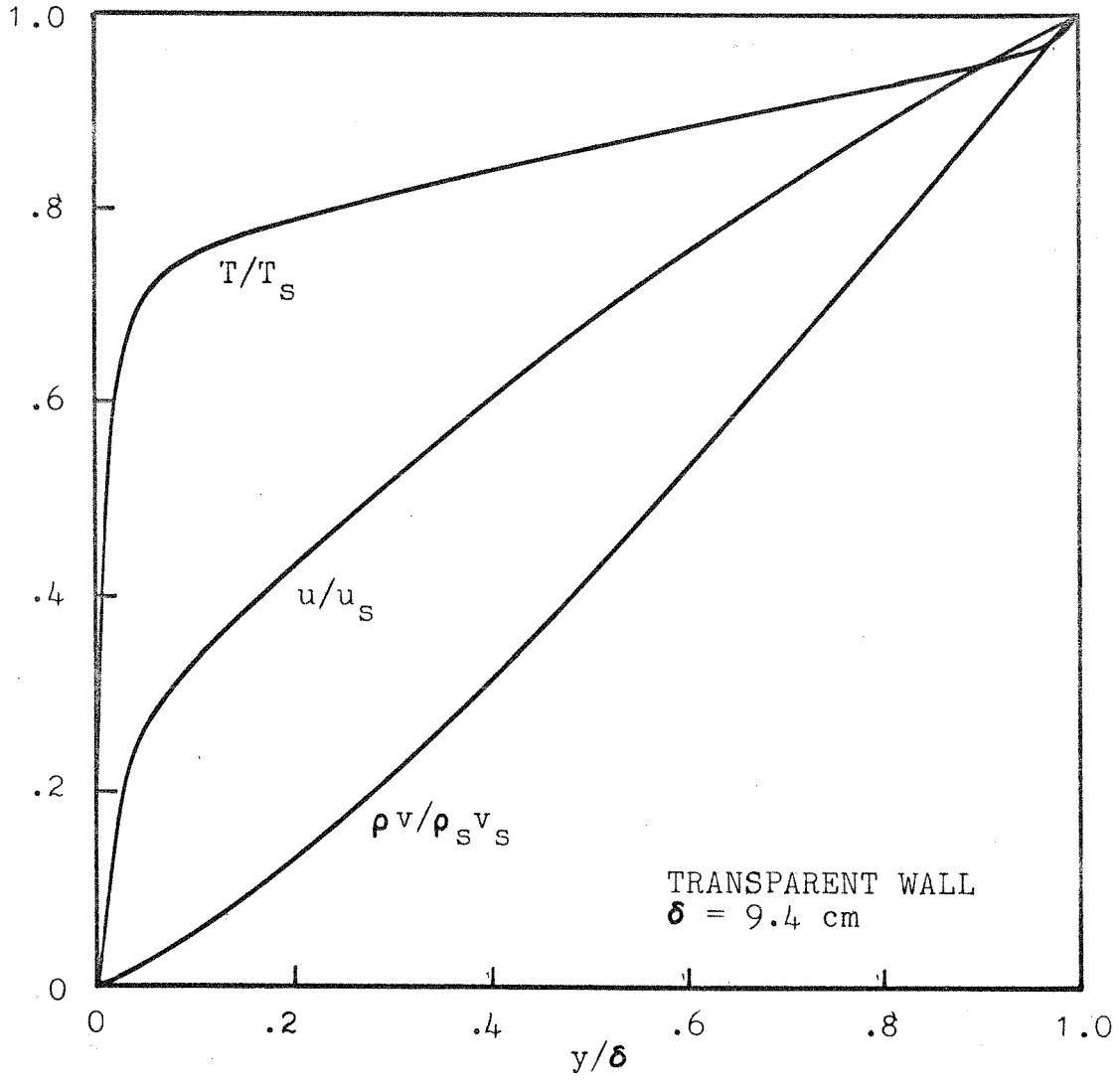

FIGURE 4. SHOCK LAYER FLOW FIELD FOR 10.0 FOOT NOSE RADIUS WITH NO BLOWING

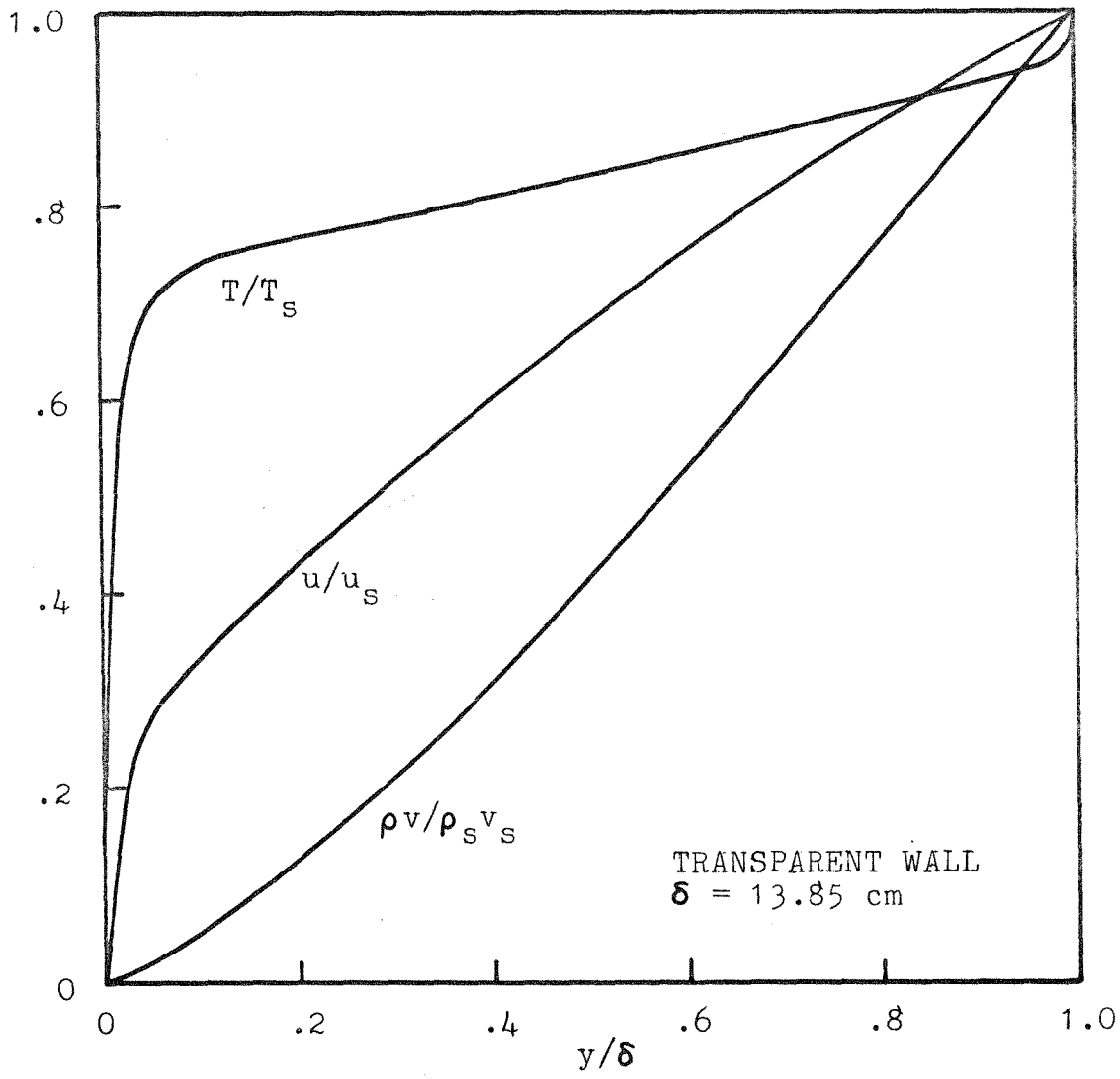

FIGURE 5. SHOCK LAYER FLOW FIELD FOR 15.0 FOOT NOSE RADIUS WITH NO BLOWING

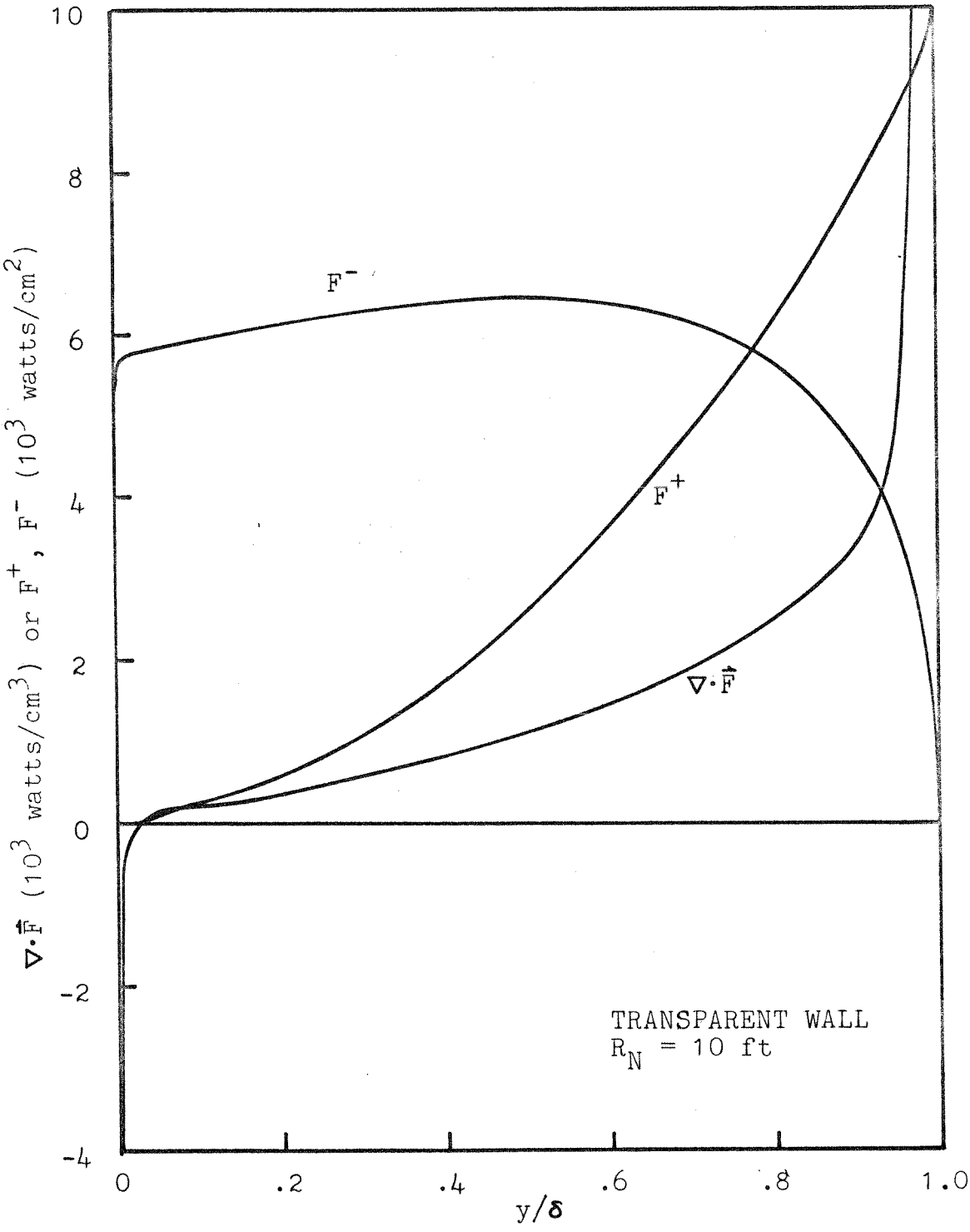

FIGURE 6. VARIATION OF NET EMISSION AND ONE-SIDED FLUXES ACROSS SHOCK LAYER WITH NO BLOWING

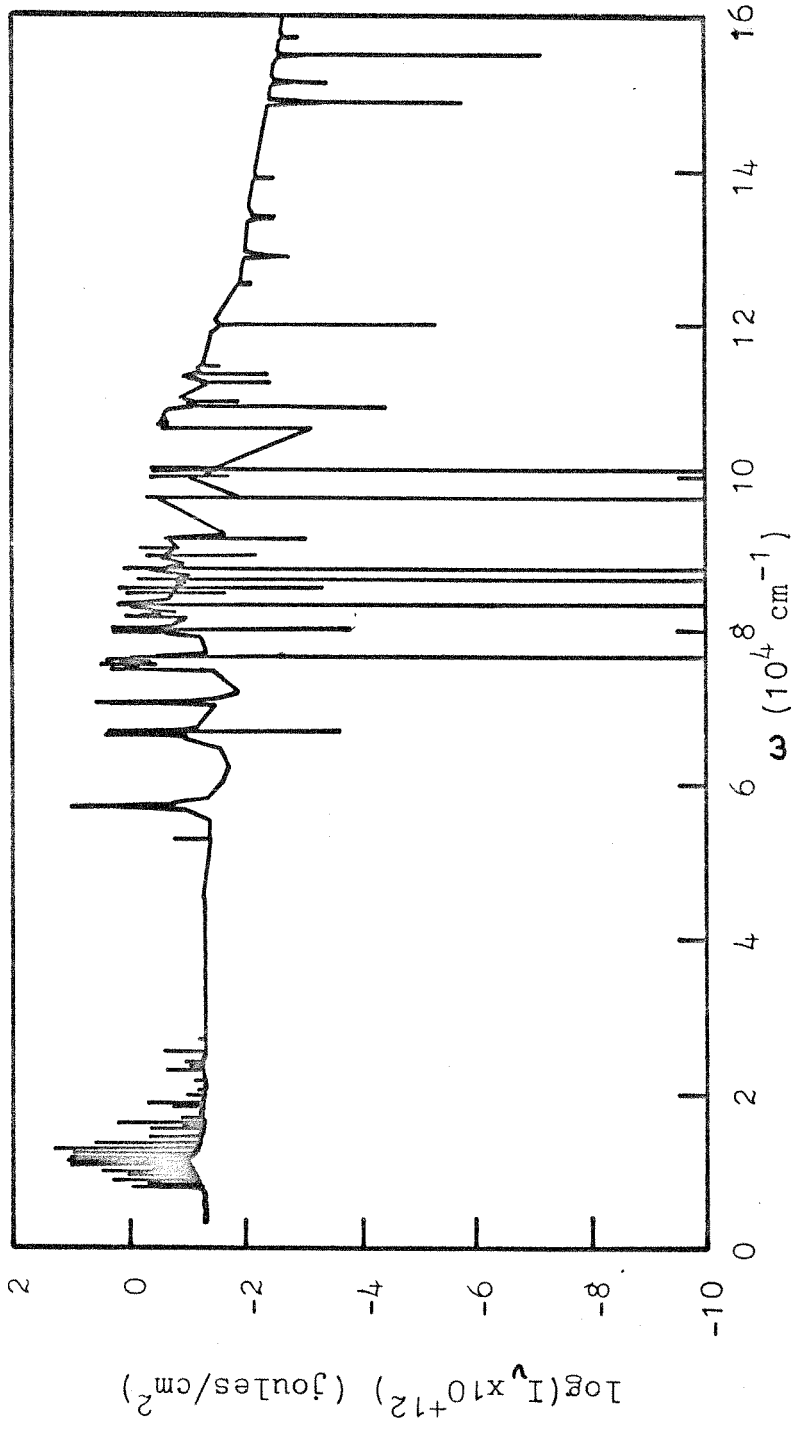

FIGURE 7. SPECTRAL RADIATION INCIDENT NORMAL TO WALL FOR 1.0 FOOT NOSE RADIUS WITH NO BLOWING

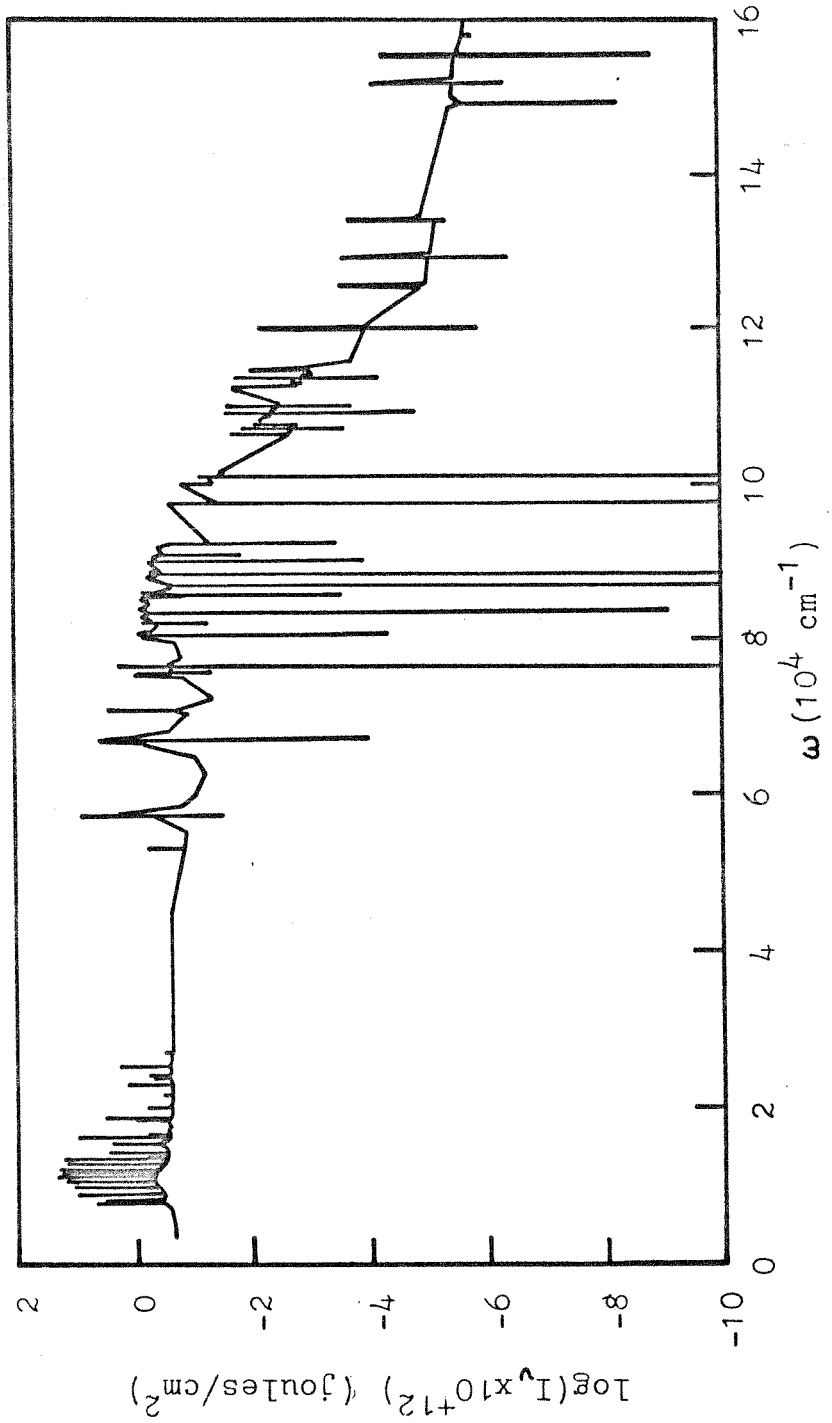

FIGURE 8. SPECTRAL RADIATION INCIDENT NORMAL TO WALL FOR 10.0 FOOT NOSE RADIUS WITH NO BLOWING

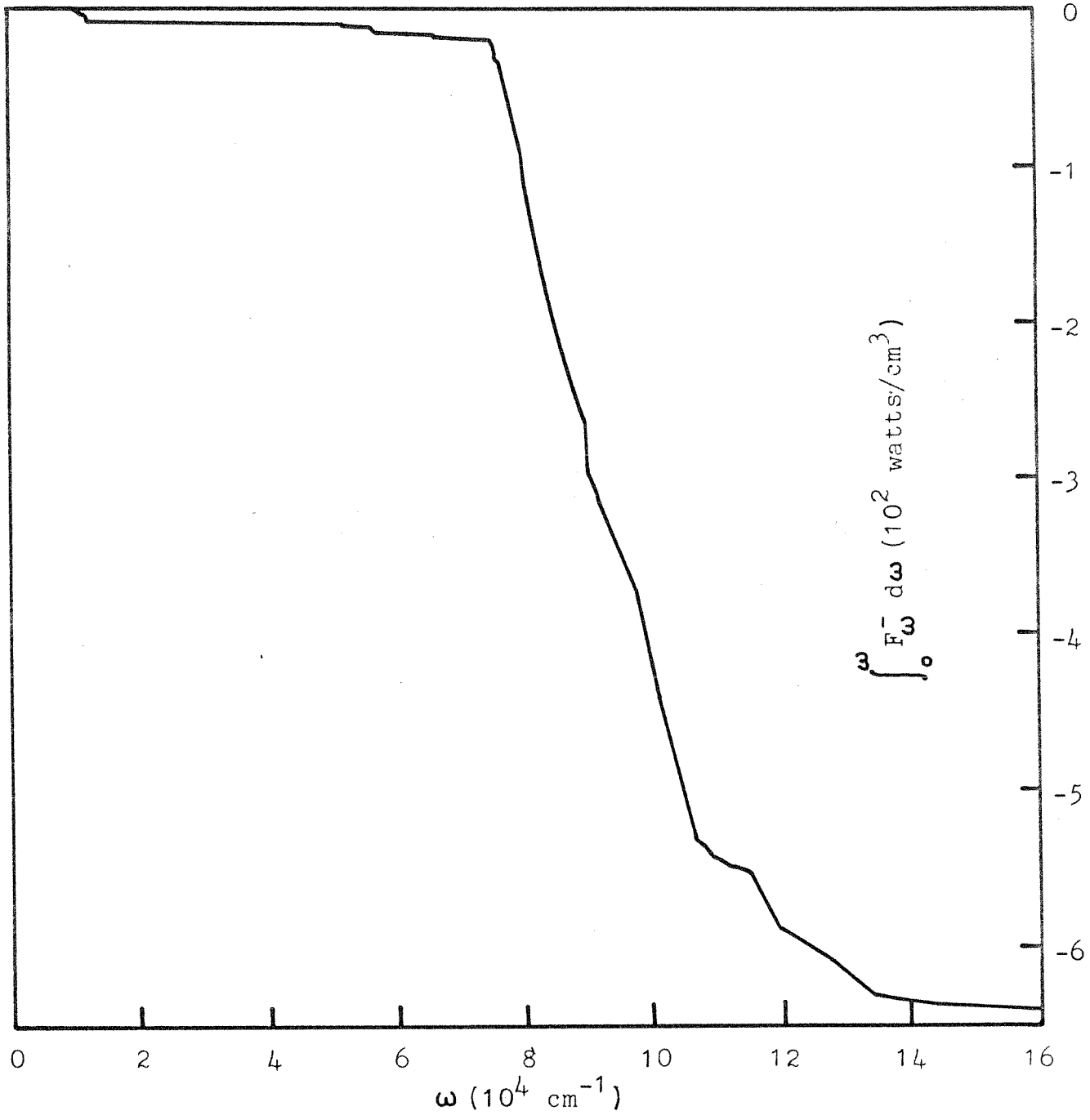

FIGURE 9. INTEGRATED $\nabla \cdot \vec{F}$ FOR SHOCK-LAYER RADIATION TRAVELING TOWARD THE WALL, EVALUATED 0.11 CM FROM THE WALL

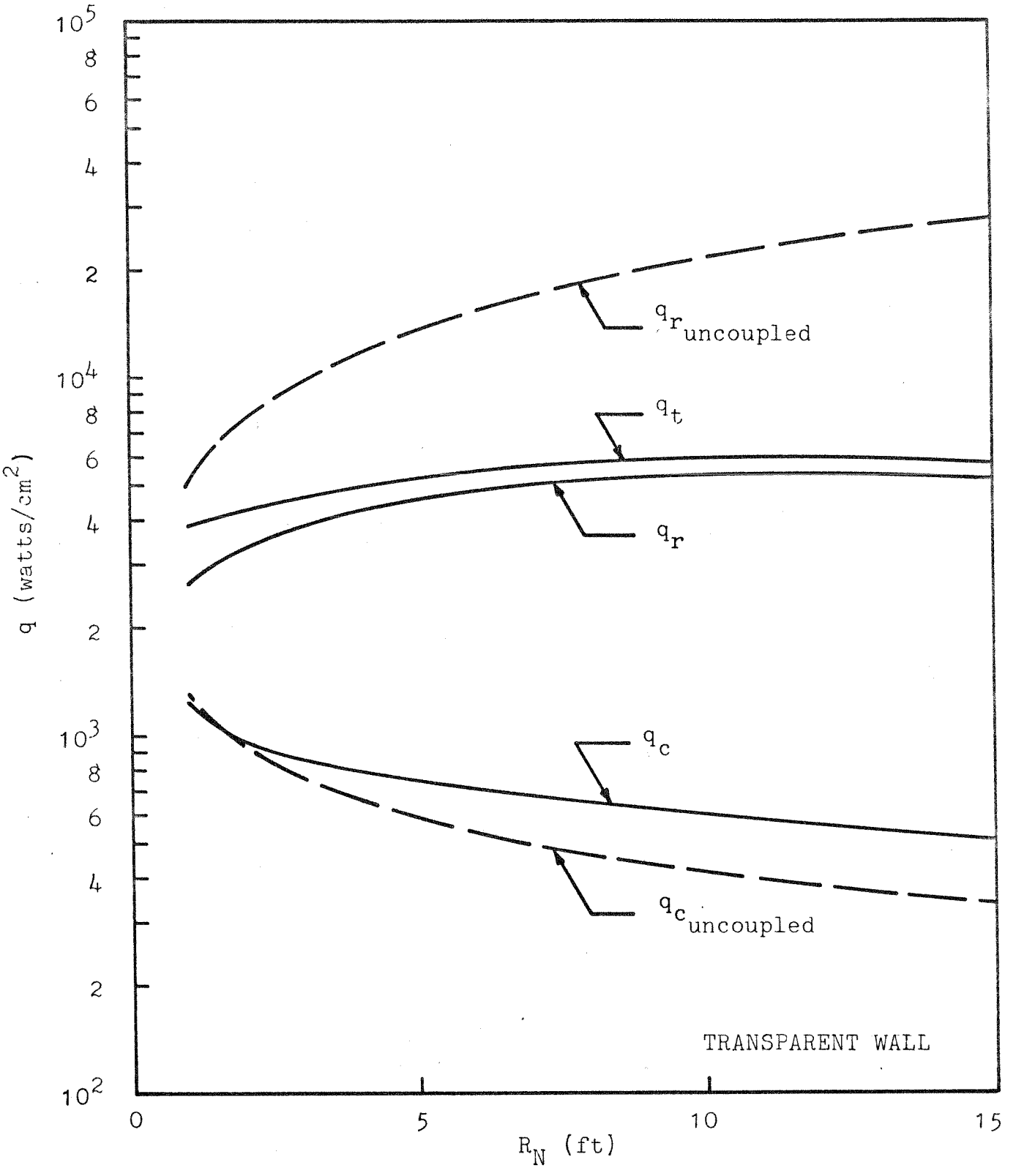

FIGURE 10. HEAT TRANSFER RATES AS A FUNCTION OF NOSE RADIUS WITH NO BLOWING

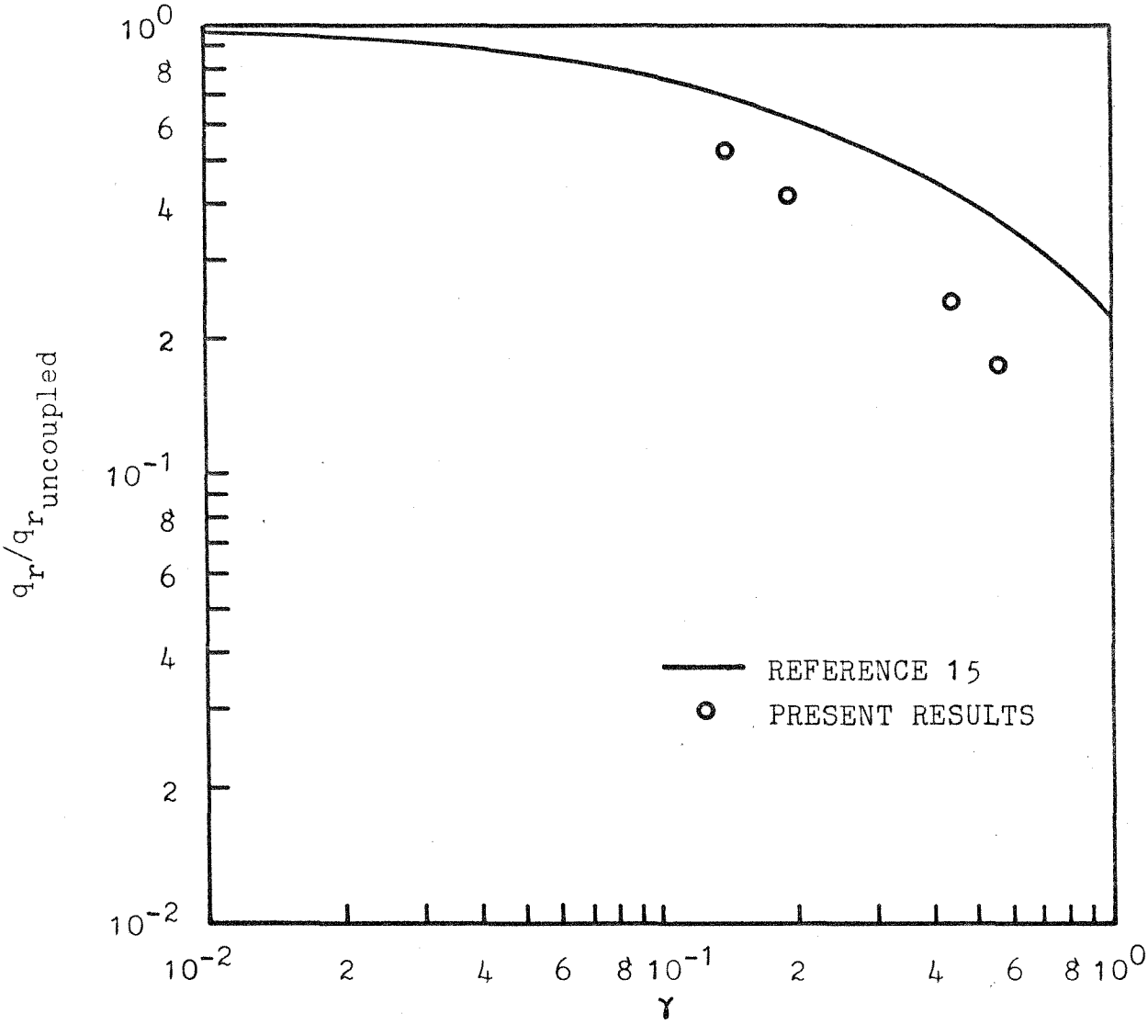

FIGURE 11. REDUCTION IN RADIATIVE FLUX TO WALL DUE TO RADIATIVE AND CONVECTIVE COUPLING

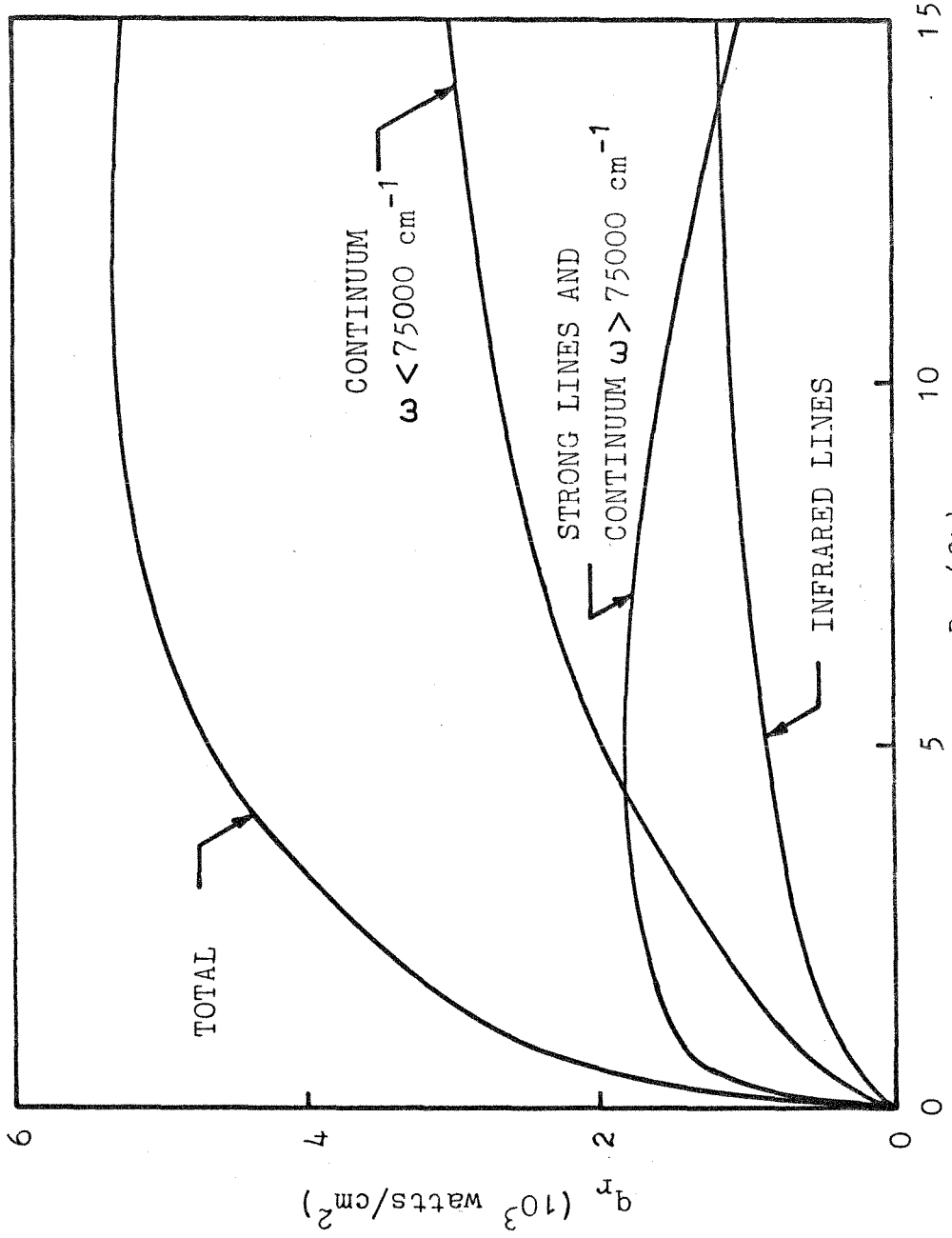

FIGURE 12. COMPOSITION OF RADIATIVE HEAT FLUX AT THE WALL AS A FUNCTION OF NOSE RADIUS

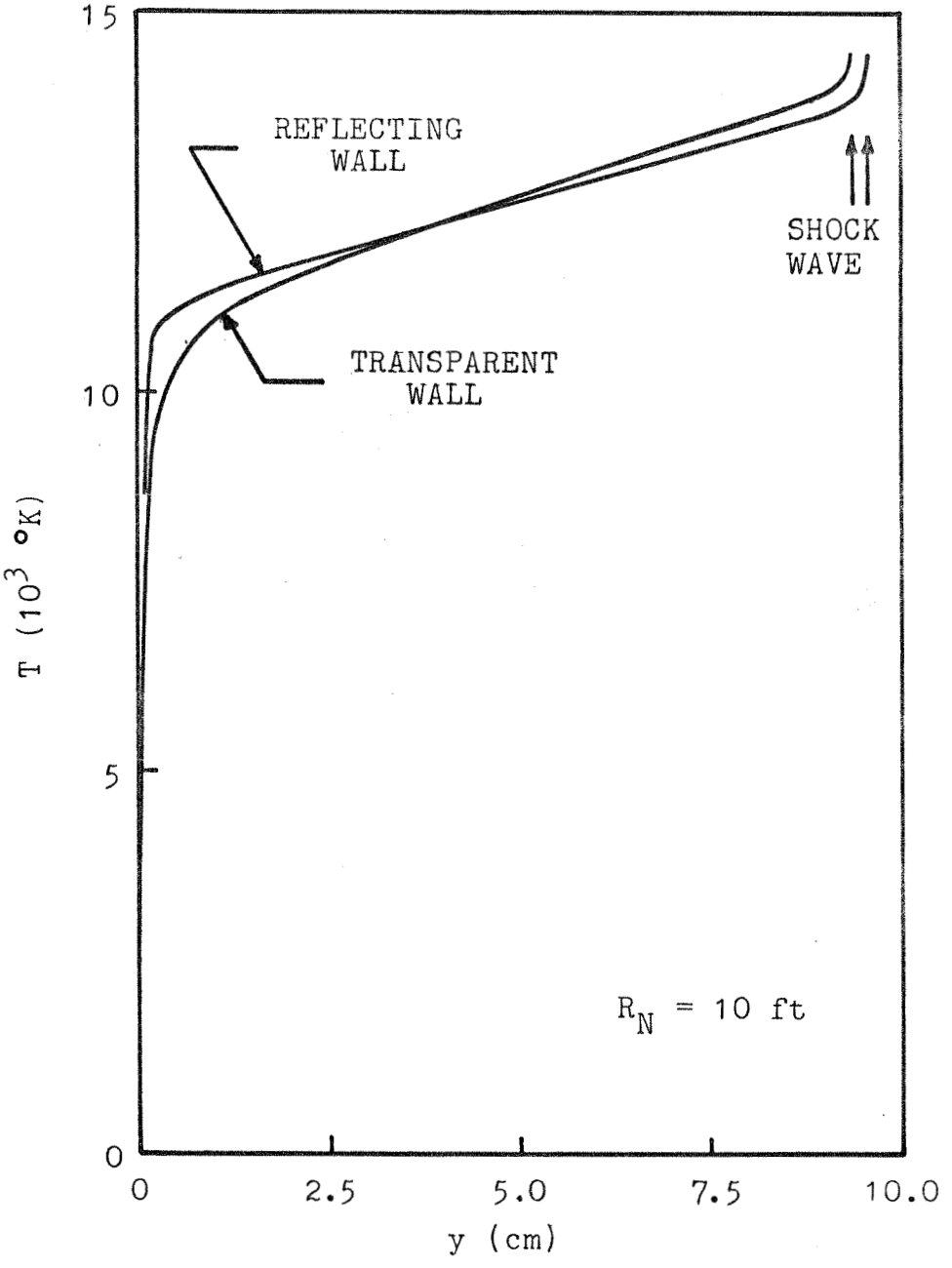

FIGURE 13. SHOCK LAYER TEMPERATURE PROFILES SHOWING THE EFFECT OF WALL REFLECTIVITY

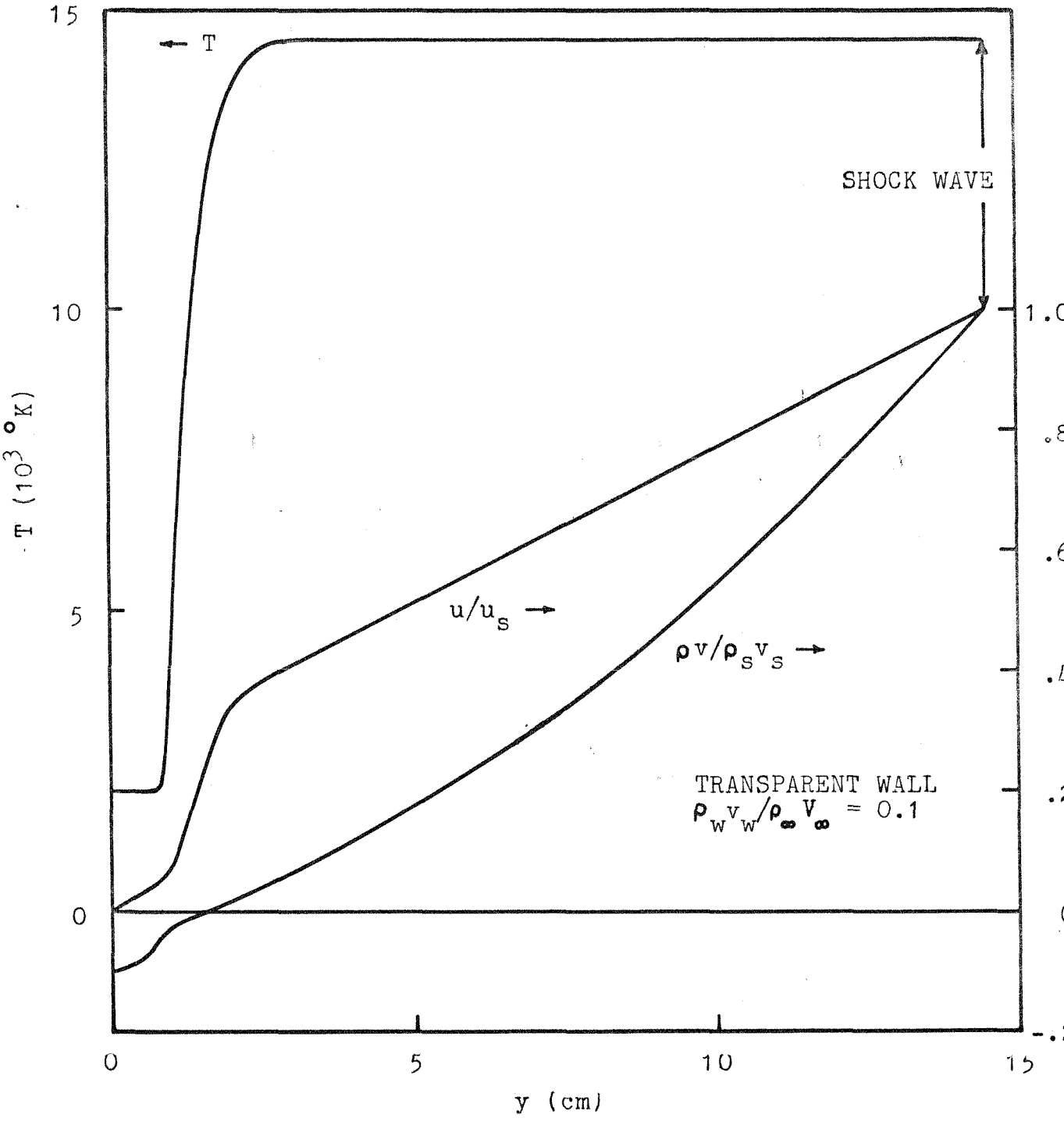

FIGURE 14. UNCOUPLED FLOW FIELD SOLUTION FOR 10.0 FOOT NOSE RADIUS WITH BLOWING

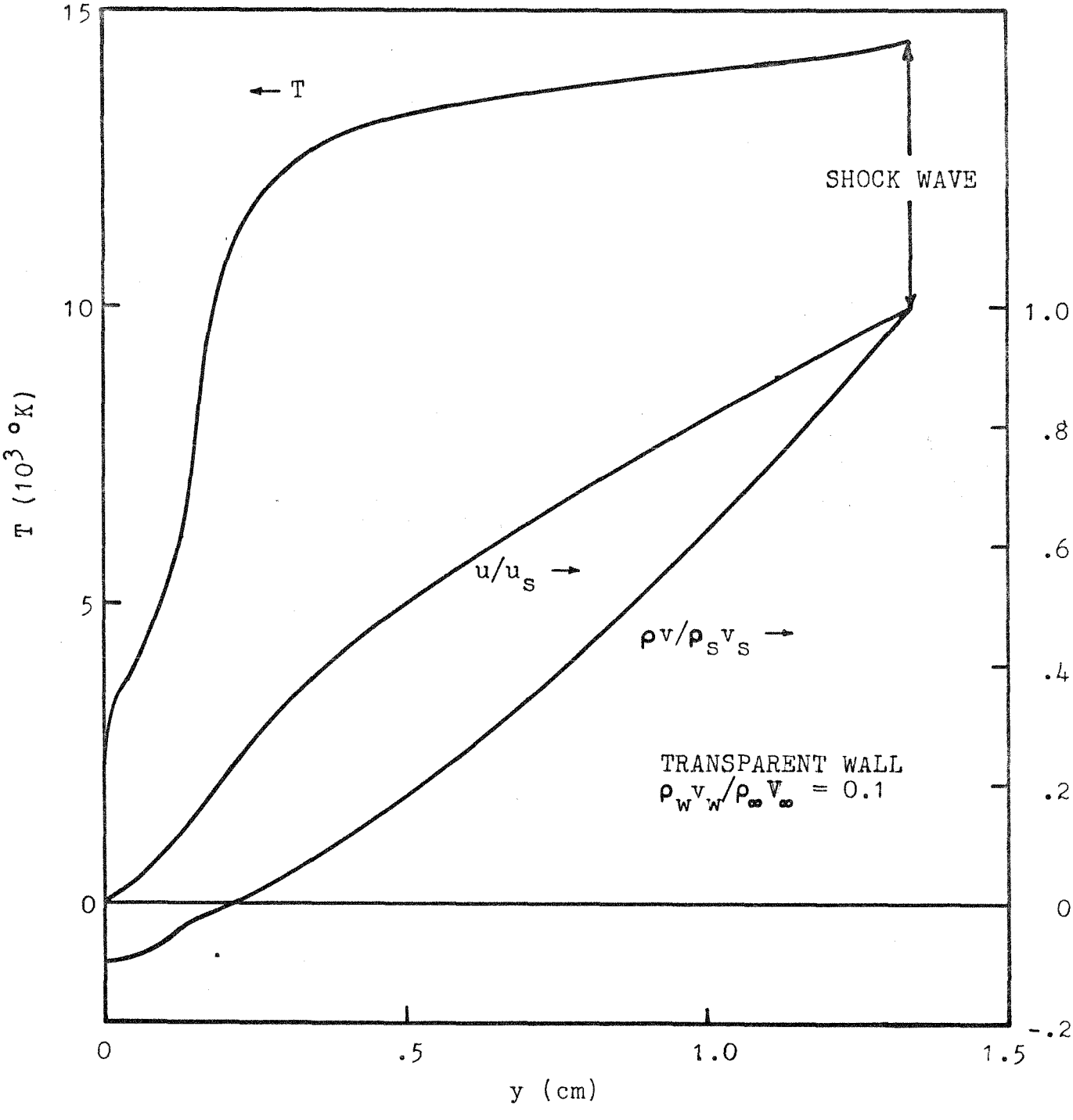

FIGURE 15. SHOCK LAYER FLOW FIELD FOR 1.0 FOOT NOSE RADIUS WITH BLOWING

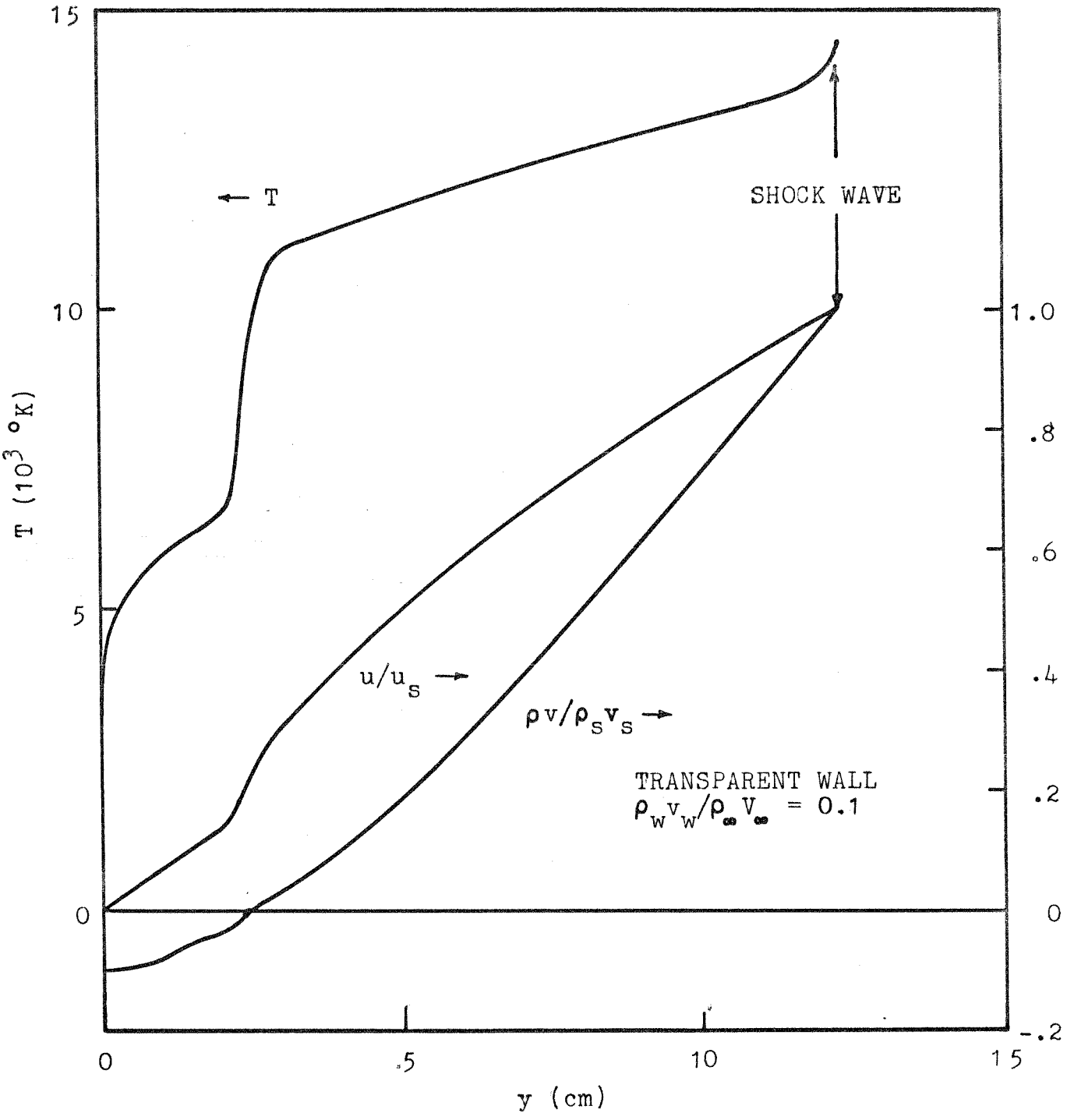

FIGURE 16. SHOCK LAYER FLOW FIELD FOR 10.0 FOOT NOSE RADIUS WITH BLOWING

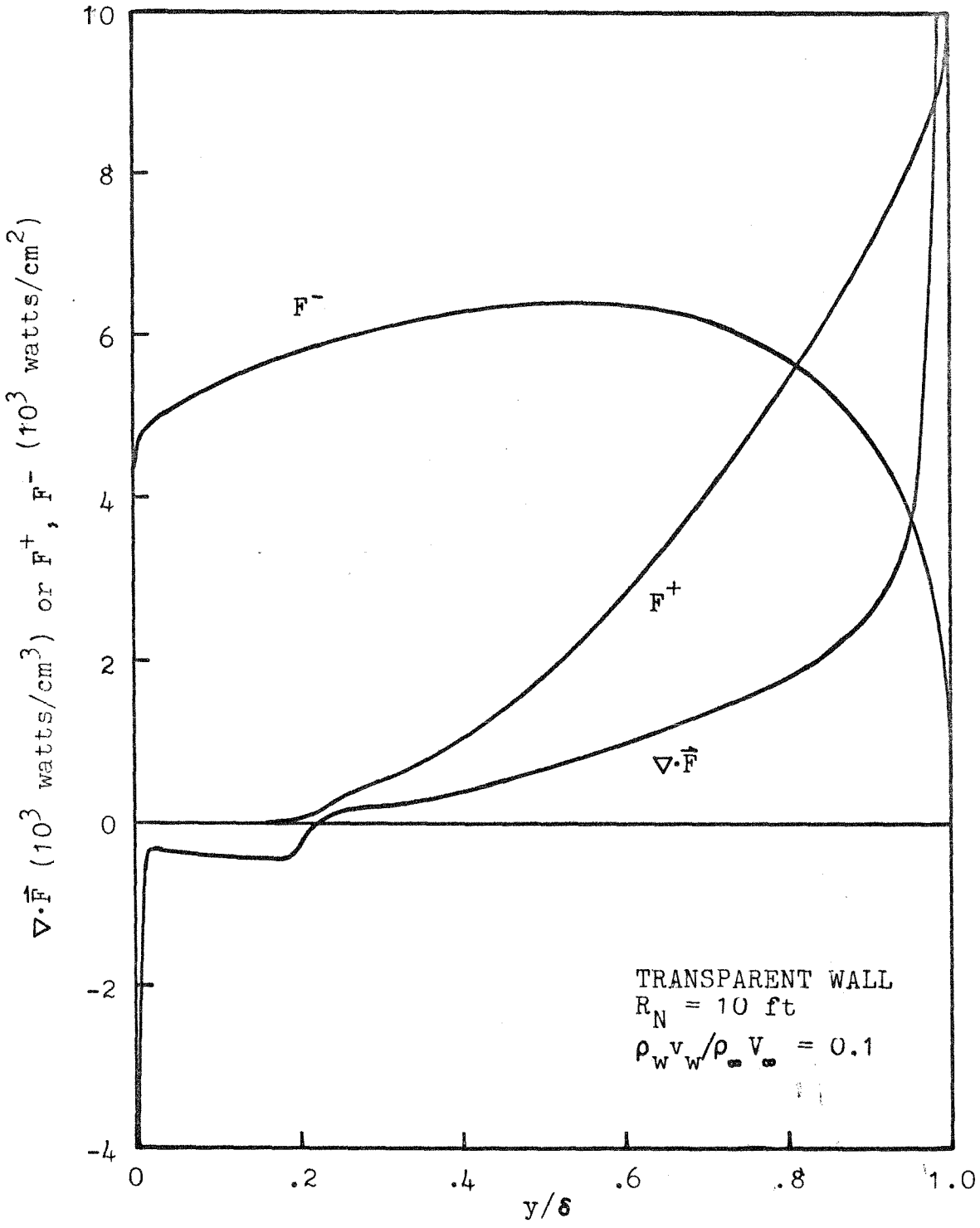

FIGURE 17. VARIATION OF NET EMISSION AND ONE-SIDED FLUXES ACROSS SHOCK LAYER WITH BLOWING

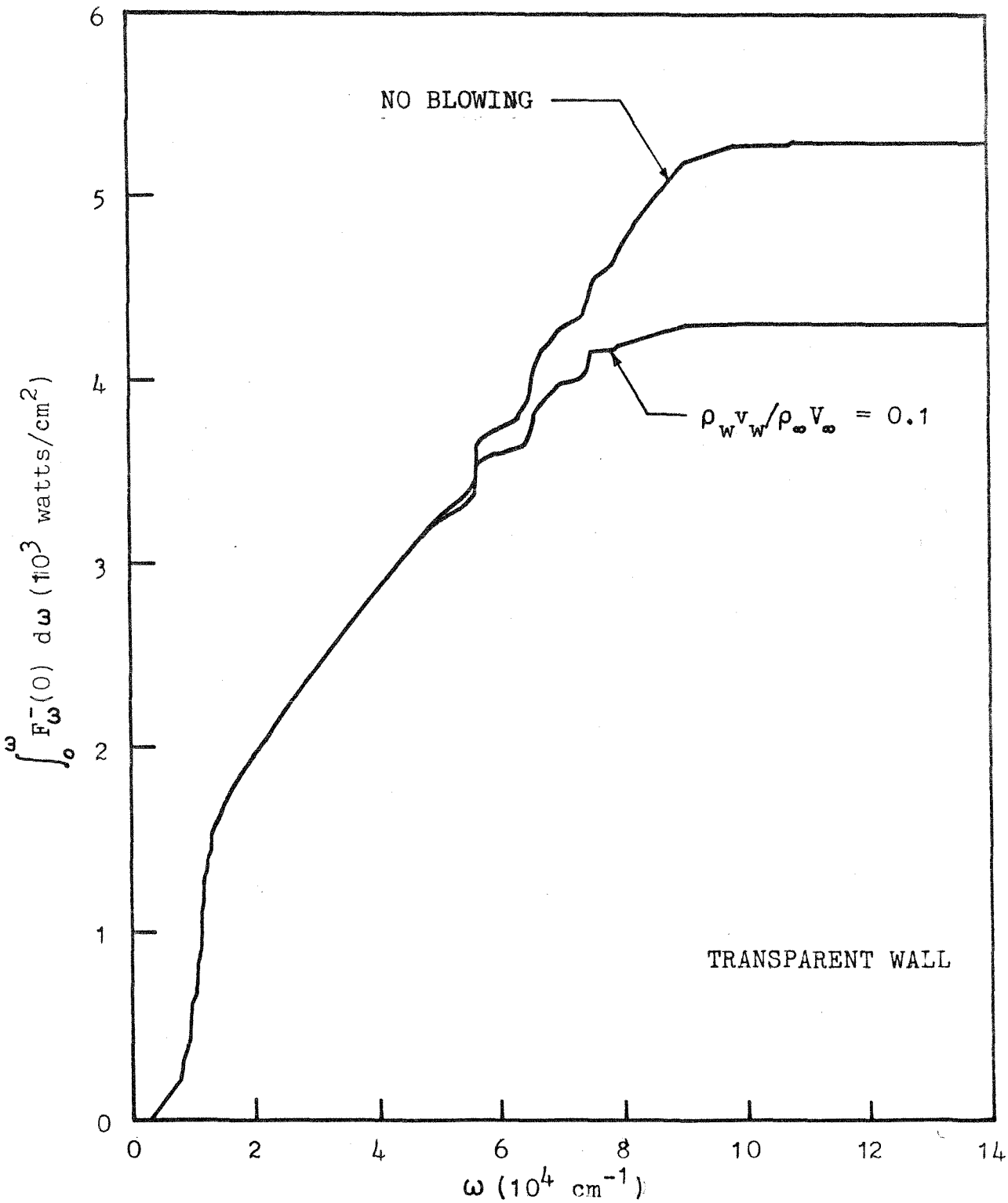

FIGURE 18. SPECTRAL CONTRIBUTION TO THE RADIATIVE HEAT TRANSFER RATE FOR 10.0 FOOT NOSE RADIUS

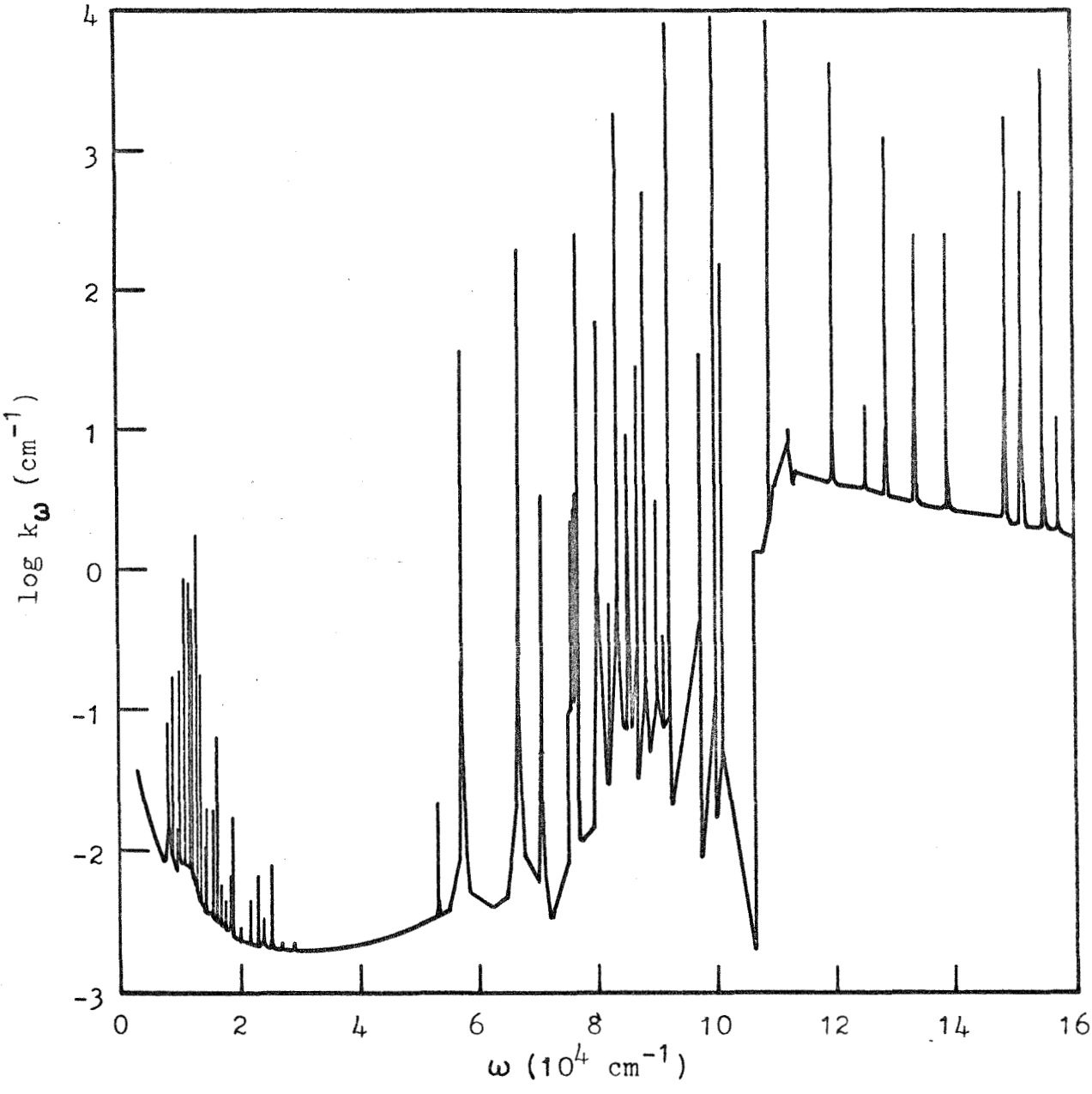

FIGURE 19. ABSORPTION COEFFICIENT OF AIR AT 1 ATM PRESSURE AND 15000 °K